Ion Mobility Mass Spectrometry of Au$_{25}$(SCH$_2$CH$_2$Ph)$_{18}$ Nanoclusters

Laurence A. Angel,[†,]* Lance T. Majors,[‡] Asantha C. Dharmaratne,[‡] and Amala Dass[‡,]*

[†]Department of Chemistry, Texas A&M University-Commerce, Texas 75429 and [‡]Department of Chemistry and Biochemistry, University of Mississippi, University, Mississippi 38677

ABSTRACT Ion mobility mass spectrometry (IM-MS) can separate ions based on their size, shape, and charge as well as mass-to-charge ratios. Here, we report experimental IM-MS and IM-MS/MS data of the Au$_{25}$(SCH$_2$CH$_2$Ph)$_{18}^-$ nanocluster. The IM-MS of Au$_{25}$(SCH$_2$CH$_2$Ph)$_{18}^-$ exhibits a narrow, symmetric drift time distribution that indicates the presence of only one structure. The IM-MS/MS readily distinguishes between the fragmentation of the outer protecting layer, made from six [$-$SR$-$Au$-$SR$-$Au$-$SR$-$] "staples' where R = CH$_2$CH$_2$Ph, and the Au$_{13}$ core. The fragmentation of the staples is characterized by the predominant loss of Au$_4$(SR)$_4$ from the cluster and the formation of eight distinct bands. The consecutive eight bands contain an increasing variety of Au$_l$S$_m$R$_n^-$ product ions due to the incremental fragmentation of the outer layer of Au$_{21}$X$_{14}^-$, where X = S or SCH$_2$CH$_2$Ph. The mobility of species in each individual band shows that the lower mass species exhibit greater collision cross sections, facilitating the identification of the Au$_l$S$_m$R$_n^-$ products. Below the bands, in the region 1200$-$2800 m/z, product ions relating to the fragmentation of the Au$_{13}$ core can be observed. In the low mass 50$-$1200 m/z region, fragment ions such as Au(SR)$_2^-$, Au$_2$(SR)$_3^-$, Au$_3$(SR)$_4^-$, and Au$_4$(SR)$_5^-$ are also observed, corresponding to the large fragments Au$_{25-x}$(SR)$_{18-(x+1)}$. The study shows that most of the dominant large fragments are of the general type Au$_{21}$X$_{14}^{\mp}$, and Au$_{17}$X$_{10}^{\mp}$ with electron counts of 8 and 6 in negative and positive mode, respectively. This suggests that geometric factors may outweigh electronic factors in the selection of Au$_{25}$(SR)$_{18}$ structure.

KEYWORDS: Au$_{25}$ nanoclusters · ion mobility · electrospray ionization · mass spectrometry · traveling-wave ion guide

Molecular thiolated gold nanoclusters contain a distinct number of core gold atoms and protecting thiolate ligands and possess extraordinary stability making them accessible to wide ranging applications.[1,2] Au$_{25}$(SCH$_2$CH$_2$Ph)$_{18}$ is the most studied nanocluster[3] because of its stability[4] and relative ease in obtaining pure nanocluster by solvent fractionation. Au$_{25}$ nanoclusters display interesting electrochemical,[2] optical,[5] magnetic,[6,7] and chiral properties;[8,9] finding application in cancer imaging[10] and catalysis.[11,12] The formula Au$_{25}$(SR)$_{18}$ was first shown using electrospray ionization mass spectrometry (ESI-MS).[13] Subsequent high resolution ESI,[14,15] matrix-assisted laser desorption ionization[16] (MALDI-MS), fast atom bombardment (FAB),[17] and collision-induced dissociation (CID) studies[18] have established its composition and molecular formula unambiguously.[19] Au$_{38}$(SR)$_{24}$ and Au$_{144}$(SR)$_{60}$ were also identified by ESI mass spectrometry.[20−22] Single crystal X-ray diffraction studies[3,5,23,24] (XRD) have revealed the crystal structures of Au$_{25}$(SCH$_2$CH$_2$Ph)$_{18}$, Au$_{38}$(SCH$_2$CH$_2$Ph)$_{24}$, and Au$_{102}$(SC$_6$H$_4$COOH)$_{44}$. The crystal structure of Au$_{25}$(SR)$_{18}$ reveals a Au$_{13}$ core and six [$-$SR$-$Au$-$SR$-$Au$-$SR$-$] staple moieties stellated on 12 of the 20 faces of the icosahedron. Density functional theory has also shown that this structure is energetically favorable.[25] XRD studies, however, are only indicative of selective crystals that were formed from the bulk sample and do not necessarily show a true representation of the entire sample. For instance, it is not clear that the crystallization of Au$_{25}$(SR)$_{18}$ and its subsequent XRD analysis represents the only possible crystal structure synthesized by the modified Brust reaction. Moreover, the gold nanoclusters Au$_{68}$(SR)$_{34}$,

Au$_{144}$(SR)$_{60}$, and Au$_{146}$(SR)$_{59}$ have not been successfully crystallized to date, and their structures are still unknown. Recently, Murray and co-workers[22] reported the two closely related formulas of Au$_{144}$(SR)$_{60}$ and Au$_{146}$(SR)$_{59}$. Many important questions remain for gold nanocluster research such as: Is the reported Au$_{25}$(SR)$_{18}$ crystal structure the only possible structure of *all* the species in solution? Can the other theoretically predicted Au$_{25}$(SR)$_{18}$ structural isomers be observed in experimental investigations?[26,25] Do Au$_{25}$ nanoclusters protected by hexanethiol and glutathione have the same structure as Au$_{25}$(SCH$_2$CH$_2$Ph)$_{18}$? It has been suggested that the Au$_{25}$ cluster containing either 18 $-$SCH$_2$CH$_2$Ph or glutathione ligands have the same structural arrangement.[27] Here, using electrospray
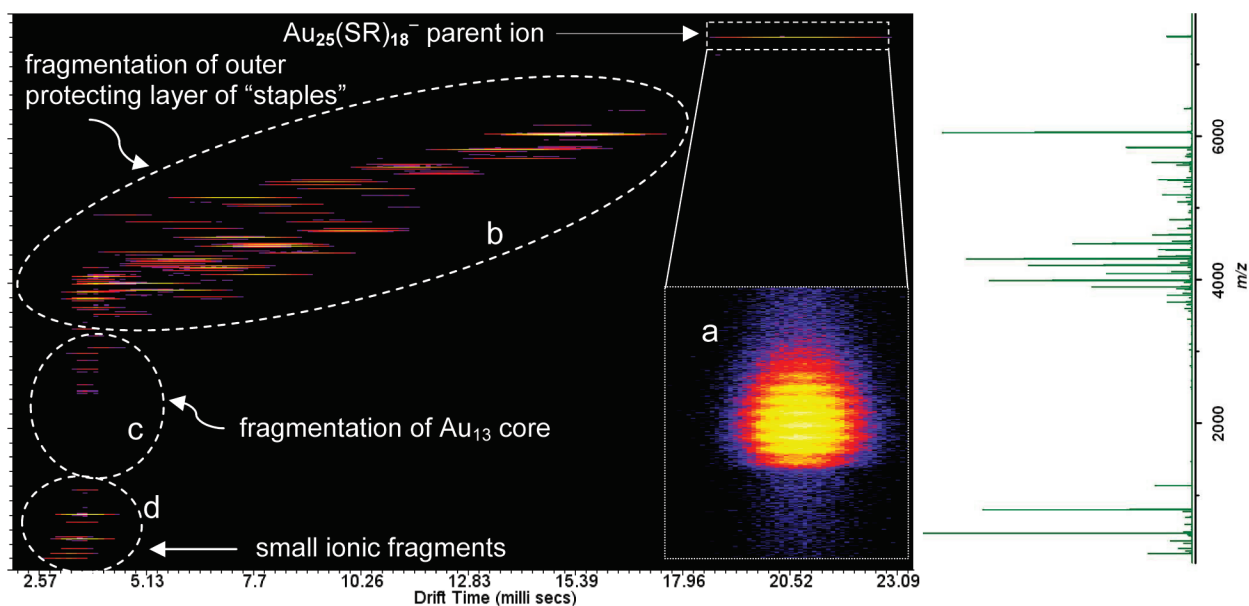
Figure 1. IM-MS/MS driftscope plot showing *m/z* (*y* axis) *versus* drift time (*x* axis) for the analysis of $Au_{25}(SCH_2CH_2Ph)_{18}^-$. Inset a shows a blow-up of isotopic distribution of the parent ion, $Au_{25}(SCH_2CH_2Ph)_{18}^-$. The CID of $Au_{25}(SCH_2CH_2Ph)_{18}$ results in the fragmentation of the $[-SR-Au-SR-Au-SR-]$ staples as shown by the slant oval b. Fragmentation of the $Au_{13}(SR)_m(S)_n$ core is shown by the vertical oval c, and the small ionic fragments are shown by d.

ionization-ion mobility-mass spectrometry (ESI-IM-MS), we present mass and structural analysis of $Au_{25}(SCH_2CH_2Ph)_{18}^-$ and its CID fragments that provide a promising technique for addressing some of the challenges in gold nanoclusters.

Unlike XRD, ESI-IM-MS analyzes the ensemble of the nanoclusters in the sample. It distinguishes between isomers and provides structural information on the conformations of gold nanoclusters that are difficult to crystallize. ESI-IM-MS is capable of separating isomeric ions that differ in their collision cross-section. It can separate samples by size, shape, and charge as well as mass.[28] Separation is achieved by measuring the time it takes an ion to migrate through a buffer gas. Ion mobility has been successfully applied to the characterization of a wide range of chemical species including polymers,[29−32] macrocycles,[33,34] isomeric oligosaccharides,[35] conformational states of proteins,[36−42] and the analysis of phospholipids and peptides.[28,43−46] The original CID MS/MS study[18] of $Na_xAu_{25}(SCH_2CH_2Ph)_{18−y}(S(C_2H_4O)_5CH_3)_y$ by Murray and co-workers reported the involvement of the semiring Au_2L_3 in the dissociation of the nanoparticle's protecting mixed monolayer. The low mass fragments of AuL_2, Au_2L_3, Au_3L_3, and Au_4L_4 were also detected by utilizing Na^+ to ionize neutral and negatively charged species at the PEG thiol ligand sites. In the present study, the inherent negative charge state of the Au_{25} nanoparticle is utilized, and an extended range of 50−8000 *m/z* in combination with isotopic resolution of all the peaks has enabled the study of a wider range of fragments in detail. The IM-MS/MS, moreover, separates the complex spectrum into various bands and facilitates the analysis of the product ions. Recently, MALDI-IM-MS

was used to analyze low mass Au-thiolate fragments generated from Au nanoparticles.[47] Gold nanoclusters have not been studied by ESI-IM-MS to the best of our knowledge. The instrument used here combines tandem quadrupole and time-of-flight mass spectrometry (Q-TOF), with traveling-wave ion mobility (IM) technology providing a powerful tool for analyzing gold nanoclusters. The Q-IM-TOF configuration provides wide *m/z* coverage so all product ions from the collision-induced dissociation of <30000 *m/z* parent ion can be observed. Product ions are also resolved by their mobility in a traveling-wave ion guide that is dependent on the physical shape of the species. Here we report the first complete Q-IM-TOF mass and mobility analysis of the collision-induced dissociation of the $Au_{25}(SCH_2CH_2Ph)_{18}^-$ nanocluster. The relationship of the $Au_{25}(SCH_2CH_2Ph)_{18}^-$ structure and the IM-MS/MS analysis lays the foundations for studying the unknown structures of a wide-range of thiolated gold nanoclusters.

RESULTS AND DISCUSSION

Survey scans of the $Au_{25}(SCH_2CH_2Ph)_{18}$ sample in both negative and positive ion mode showed the $Au_{25}(SCH_2CH_2Ph)_{18}^-$ and $Au_{25}(SCH_2CH_2Ph)_{18}(TOA)_2^+$ ions were the dominant observable ions in the sample, where TOA represents the tetraoctylammonium cation. This is consistent with $Au_{25}(SCH_2CH_2Ph)_{18}^-$ having an intrinsic negative charge. However, in the positive ion mode both the $Au_{25}(SCH_2CH_2Ph)_{18}(TOA)^+$ and $Au_{25}(SCH_2CH_2Ph)_{18}^+$ ions were also observed but at lower signal than the $Au_{25}(SCH_2CH_2Ph)_{18}(TOA)_2^+$ ion (Supporting Information). The reducing condition during synthesis lead to the preferential formation of

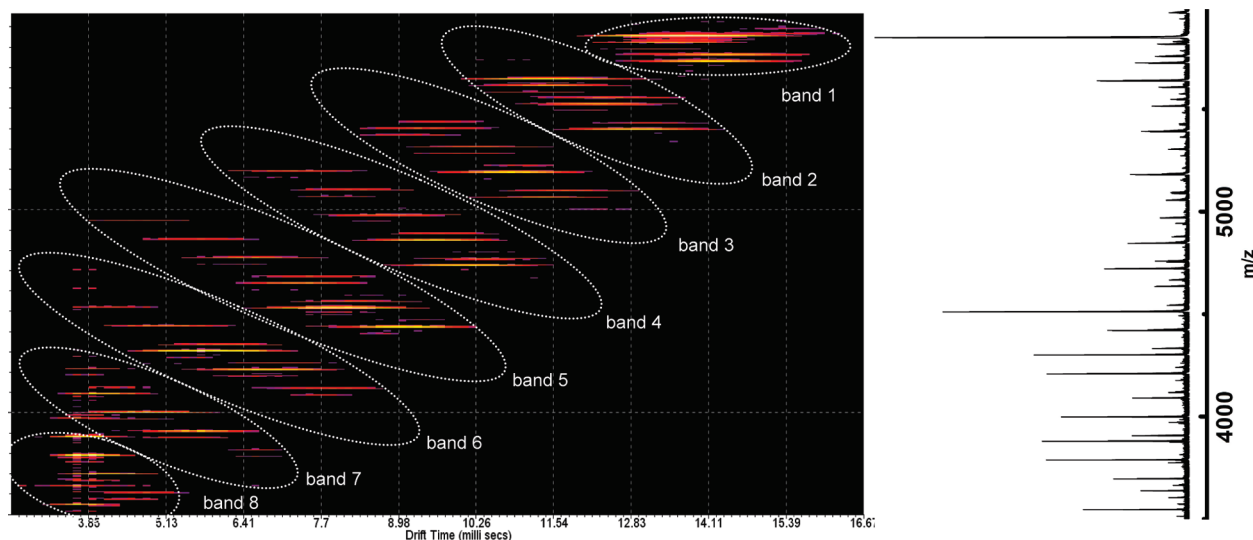**Figure 2. The IM-MS/MS driftscope plot (mass range: 3500−6000 *m/z*) of Au$_{25}$(SCH$_2$CH$_2$Ph)$_{18}^-$ is marked by distinct bands, 1−8. The species in each band show the same dependency of decreasing mobility with lower mass in contrast to the more usual inverse dependency. These bands facilitate in the identification of the products ions. In the MS/MS spectrum (shown right), these species are mixed together complicating the interpretation of the spectrum.**

Au$_{25}$(SCH$_2$CH$_2$Ph)$_{18}$(TOA)$_2^+$ with some additional oxidation states present in solution.[48] This article focuses on the IM-MS/MS of Au$_{25}$(SCH$_2$CH$_2$Ph)$_{18}^-$ and MS/MS analysis of both Au$_{25}$(SCH$_2$CH$_2$Ph)$_{18}^+$ and Au$_{25}$(SCH$_2$CH$_2$Ph)$_{18}^-$ species. Figure 1 shows the driftscope plot of *m/z* versus drift time of the IM-MS/MS of Au$_{25}$(SCH$_2$CH$_2$Ph)$_{18}^-$ taken by resolving the Au$_{25}$(SCH$_2$CH$_2$Ph)$_{18}^-$ parent ion and applying 100 V lab kinetic energy to the trap T-wave cell. Under these optimal CID conditions a wide range of fragment ions are produced from the parent Au$_{25}$(SCH$_2$CH$_2$Ph)$_{18}^-$ nanoclusters. The MS/MS plot of the fragmentation of Au$_{25}$(SCH$_2$CH$_2$Ph)$_{18}^-$ is shown on the right. The Au$_{25}$(SCH$_2$CH$_2$Ph)$_{18}^-$ parent ion is at the top right-hand corner at 7391 *m/z* (isotopic mass). Inset a in Figure 1 is a close-up of the *m/z* and drift time plot of the Au$_{25}$(SCH$_2$CH$_2$Ph)$_{18}^-$ parent ion. The close-up of Au$_{25}$(SCH$_2$CH$_2$Ph)$_{18}^-$ reveals the isotope pattern and a narrow, symmetric drift time distribution with a mean drift time (t) of 20.6 ms and peak width at half-maximum (Δt) of 1.9 ms. The ratio $t/\Delta t$ compares well to the 5−10 resolution of the instrument and suggests there is only one structural isomer present in the sample, Although there is a possibility that similar structural isomers remain unresolved due to the limited resolution of the instrument.[49] As discussed in more detail later, however, the IM-MS/MS fragmentation pattern is sensitive to the arrangement of the outer core "staples". Any significant rearrangement of the staples should result in an apparent drift time asymmetry of Au$_{25}$(SCH$_2$CH$_2$Ph)$_{18}^-$. Theory[25] shows that the Au$_{13}$ core with an outer protecting layer of six [−SR−Au−SR−Au−SR−] staples is the energetically favored isomer, and it is the only experimental XRD structure obtained so far. Here, the presence of well-defined drift times in the IM-MS/MS experimental data

supports that all Au$_{25}$(SCH$_2$CH$_2$Ph)$_{18}^-$ ions have the same structure as revealed by the XRD study.[3]

Figure 1 shows the rich fragmentation pattern for Au$_{25}$(SCH$_2$CH$_2$Ph)$_{18}^-$. The IM-MS/MS spectrum is dominated by products resulting from the fragmentation of the outer protecting layer of "staples" as observed in regions b and d. Region c also shows products from the fragmentation of the Au$_{13}$ core. In our discussion of the fragmentation products we will refer to the products as Au$_l$(SR)$_m$S$_n^-$, where R = −CH$_2$CH$_2$Ph. The weak product ion signal observed at the top of the fragmentation of the outer-layer staples band b, at 6389 and 6179 *m/z*, are the Au$_{22}$(SR)$_{15}^-$ and Au$_{22}$(SR)$_{13}$S$_2^-$ ions, respectively. The Au$_{22}$(SR)$_{15}^-$ relates to the loss of a Au$_3$(SR)$_3$ and the Au$_{22}$(SR)$_{13}$S$_2^-$ to the loss of a Au$_3$(SR)$_3$ and two −CH$_2$CH$_2$Ph groups. The loss of Au$_3$(SR)$_3$, however, is small in comparison to the loss of Au$_4$(SR)$_4$ which corresponds to the formation of the product ion Au$_{21}$(SR)$_{14}^-$ at 6055 *m/z*; one of the largest product peaks in the IM-MS/MS spectrum. The fragmentation of Au$_{25}$(SCH$_2$CH$_2$Ph)$_{18}^-$ is dominated by the loss of one and two Au$_4$(SR)$_4$ units which may be accompanied by additional -R fragments. The Au$_4$(SR)$_4$ unit has been observed in ESI,[18] MALDI[16] and FAB[17] MS experiments and is suggested to form as a result of a multistep rearrangement of two or more "staples" on the surface of the gold nanoparticle prior to fragmentation.[18] The formation of Au$_4$(SR)$_4$ and accompanying products is probably driven thermodynamically due to the cyclic nature of Au$_4$(SR)$_4$ as discussed in more detail later.

Starting below the Au$_{21}$(SR)$_{14}^-$ ion is a series of bands that form due to the unique chemical structure of Au$_{25}$(SCH$_2$CH$_2$Ph)$_{18}^-$. Figure 2 shows a close-up of this region and labels the bands 1−8 to facilitate in their discussion. The driftscope software allows the extraction of a mass spectrum for each individual band. Figure 3
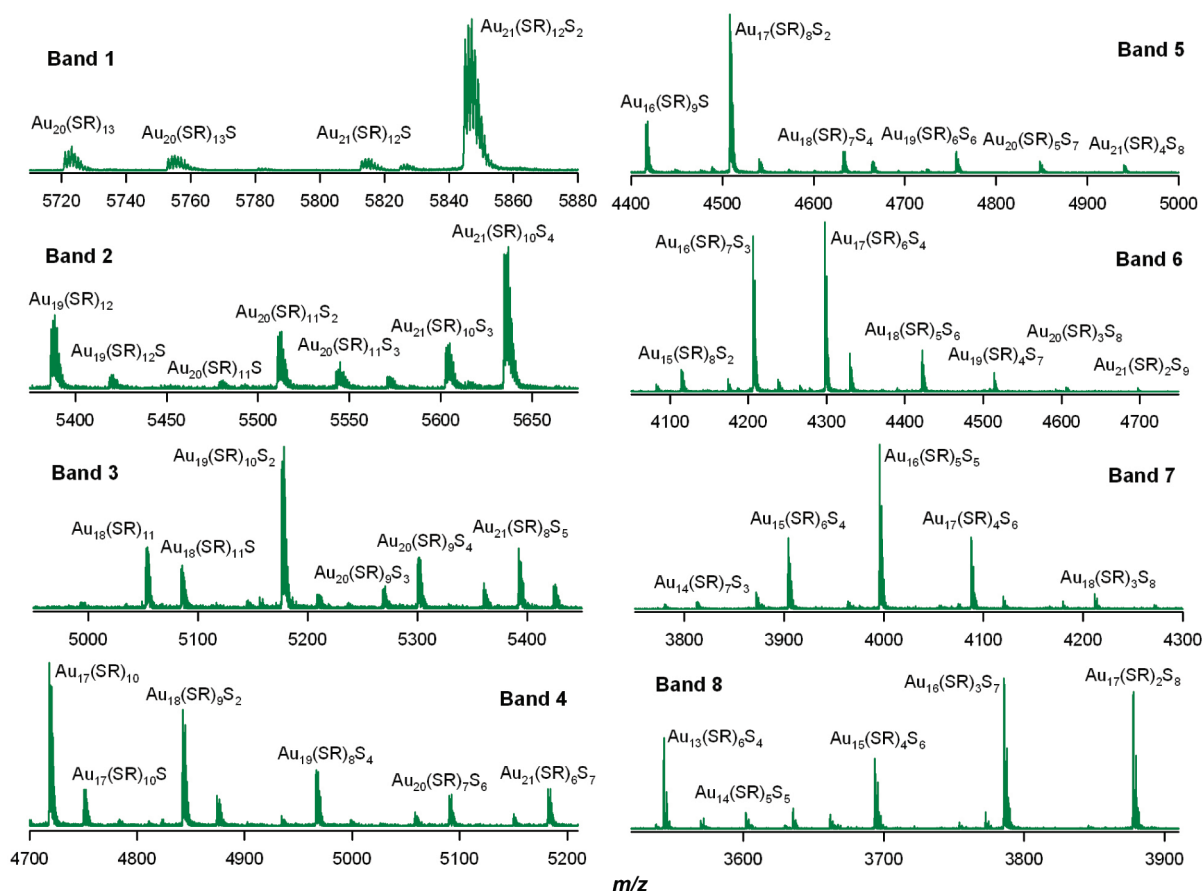
Figure 3. The extracted mass spectra of bands 1−8 present in the IM-MS/MS of $Au_{25}(SCH_2CH_2Ph)_{18}^-$ showing the identities of some of the main species. All the species are single negatively charged.

shows the extracted mass spectra of each band and shows the identities of the some of the major species present. All the bands, in Figure 2, have a negative slope slanting from left to right across the driftscope plot. The product ions are all single negatively charged species and so each of the bands are displaying an apparent direct dependence between mass and mobility; the higher masses are associated with higher mobilities (peaks on the top left of each band) and the lower masses (peaks toward the bottom right of each band) are associated with lower mobilities. This is in contrast to the usual inverse dependency between mobility and mass because the collision cross-section often decreases with

lower mass. However, in Figure 2 the reduced mobility of the lower mass species is due to an increase in the collision cross-sections overcoming the mass factor. The compact, heavier structures are on the top left of each band and the bulky, lighter structures are on the bottom right of each band. Correspondingly, the species on the top left of each band have a higher number of Au and S atoms and the species on the lower right of each band have a higher number of bulky −CH_2CH_2Ph groups. The combined mass of the Au and S atoms is greater than the mass of −CH_2CH_2Ph groups that replace

them. The replacement of Au and S atoms with −CH_2CH_2Ph, however, substantially increases the collisional cross-section of the cluster, resulting in the longer drift times.

For example, Figure 3 shows the highest mass species in band 1 is $Au_{21}(SR)_{12}S_2^-$ which also exhibits the highest mobility in the band. The lowest mass species in band 1 is $Au_{20}(SR)_{13}^-$ and exhibits the lowest mobility. The difference in the mass between $Au_{21}(SR)_{12}S_2^-$ and $Au_{20}(SR)_{13}^-$ is $\Delta m = -Au$ (197) − S (32) + R (105) = −124 amu. This −124 amu difference in mass is accompanied by an increase in the collision cross-section of $Au_{20}(SR)_{13}^-$ due to the Au and S atoms being replaced by −CH_2CH_2Ph. Across all of the eight bands Au and S atoms are replaced by −CH_2CH_2Ph ligands. Interestingly, the heaviest mass species associated with the highest mobility in bands 1−6 is of the form $Au_{21}(SR)_nS_m^-$. The compact nature of the $Au_{21}(SR)_nS_m^-$ ion coincides with the loss of $Au_4(SR)_4$ unit and the relative stability of these two products.

Another interesting observation is that the consecutive bands 1−8 display a progression in the loss of Au and gain of −CH_2CH_2Ph. For example, in band 2 the high and low mass species are $Au_{21}(SR)_{10}S_4^-$ and $Au_{19}(SR)_{12}^-$, respectively, exhibiting a loss of 2 Au and gain of 2 −CH_2CH_2Ph. The Δm across band 2 is twice
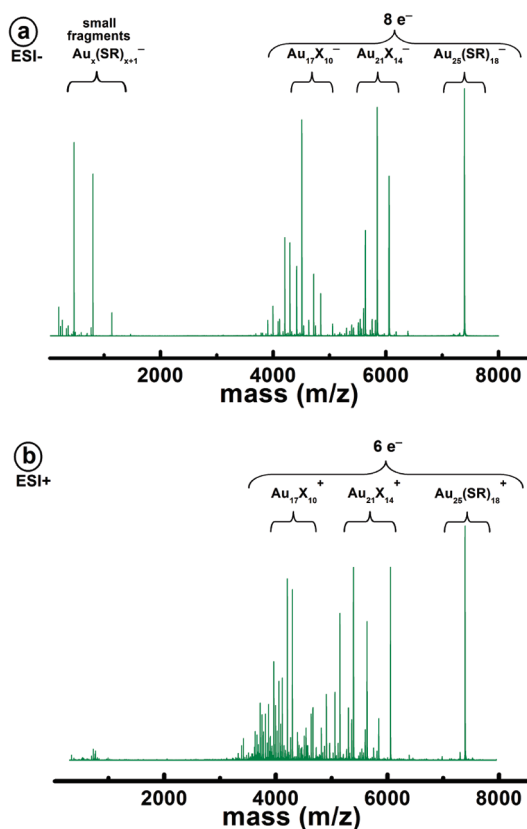
Figure 4. MS/MS of (a) $Au_{25}(SCH_2CH_2Ph)_{18}^-$; (b) $Au_{25}(SCH_2CH_2Ph)_{18}^+$. Preferential elimination of Au_4X_4 dictates the fragmentation process. The electron count of 8 and 6 are observed in negative and positive mode, respectively. X in the large fragment represents either SR or S, and $x = 1$, 2, 3, 4 in the small fragments.

that of band 1; $\Delta m = -2Au\ (396) - 2S\ (64) + 2R\ (210) = -250$ amu. Likewise, band 3 has high and low mass species of $Au_{21}(SR)_8S_7^-$ and $Au_{18}(SR)_{11}^-$ giving $\Delta m = -3Au\ (591) - 3S\ (96) + 3R\ (315) = -372$ amu. This general trend continues across bands 4–8 (Supporting Information, Table S1). The final band 8 contains a low mass species $Au_{13}(SR)_6S_4^-$ which represents the loss of 8 Au. The $Au_{13}(SR)_6S_4^-$ species has now lost all the Au atoms from the outer protecting "staple" shell and contains only Au atoms that are in the Au_{13} core with a rearrangement of stabilizing S and SR units.

$Au_{25-4x}X_{18-4x}^{\mp}$ and the Corresponding Au_4X_4 Fragments. $Au_{25}(SR)_{18}$ can be prepared either as a neutral, negative, or positive charge species based on the synthetic conditions or intentional manipulation of the charge state.[48] Figure 4 shows the MS/MS of both $Au_{25}(SCH_2CH_2Ph)_{18}^-$ and $Au_{25}(SCH_2CH_2Ph)_{18}^+$ species. For $Au_{25}(SCH_2CH_2Ph)_{18}^-$, the most intense fragments in the 5–7 kDa region are $Au_{21}(SR)_{14}$, $Au_{21}(SR)_{12}S_2$, and $Au_{21}(SR)_{10}S_4$. In terms of electronic structure, these frag-
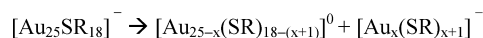
TABLE 1. Assignments of the Major Fragments in the Negative and Positive MS/MS Spectrum; n_e Indicates the Electron Shell Count of the Charged Fragment

m/z	charged fragment[a]	n_e^-, n_e^+	neutral fragment[b]
7391	$Au_{25}(SR)_{18}^{\mp}$	8, 6	-
6055	$Au_{21}(SR)_{14}^{\mp}$	8, 6	$Au_4(SR)_4$
5845	$Au_{21}(SR)_{12}S_2^{\mp}$	8, 6	$Au_4(SR)_4 + R_2$
5635	$Au_{21}(SR)_{10}S_4^{\mp}$	8, 6	$Au_4(SR)_4 + R_4$
4719	$Au_{17}(SR)_{10}^{\mp}$	8, 6	$2(Au_4(SR)_4)$
4509	$Au_{17}(SR)_8S_2^{\mp}$	8, 6	$2(Au_4(SR)_4) + R_2$
4299	$Au_{17}(SR)_6S_4^{\mp}$	8, 6	$2(Au_4(SR)_4) + R_4$
1310	$Au_4(SR)_5^-$		$Au_{21}(SR)_{13}$
1139	$Au_3(SR)_4^-$		$Au_{22}(SR)_{14}$
805	$Au_2(SR)_3^-$		$Au_{23}(SR)_{15}$
471	$Au(SR)_2^-$		$Au_{24}(SR)_{16}$

[a]The charged fragments observed in the mass spectra of Figures 4 and 6. [b]The neutral fragments corresponding to the loss of the charged species.

ments are of the basic type, $Au_{21}X_{14}$, where X represents either SCH_2CH_2Ph or S, and contain 14 electron-localizing S atoms. The fragment corresponding to the loss of $Au_4(SR)_4$ has been observed in Au_{25}[16−18] and Au_{68}[50,51] nanoclusters using the ionization methods of ESI,[18] MALDI,[16,50,51] and fast atom bombardment (FAB).[17] FAB ionization causes major cleavage in the carbon−sulfur (C−S) bond.[52] In the Au_{25} FAB analysis, competition between the C−S and the Au−S cleavage was observed and $Au_{21}(SR)_{14}$ was a minor fragment compared with other fragments.[17] However the fragmentation observed in both ESI and MALDI experiments have $Au_{21}(SR)_{14}$ as a major product.

The next principal species in the MS/MS spectrum are of the form $Au_{17}X_{10}$ coinciding with the loss of 2 neutral Au_4X_4 fragments. Grönbeck et al.[53] have shown that $Au_4(SR)_4$ forms a cyclic ring that is 2.53 eV lower in energy to the linear form for the −SMe ligands.[53] The energy of $Au_4(SR)_4$ is comparable with the larger cyclic rings of $Au_6(SR)_6$, $Au_8(SR)_8$, and $Au_{10}(SR)_{10}$, but there is no thermodynamic driving force for $Au_4(SR)_4$ to grow to these larger sizes. This has led to the prediction that $Au_4(SR)_4$ is a protecting group for the Au_{38} nanocluster.[54] Cliffel[55] and others[56−59] have also shown experimentally that $Au_4(ligand)_4$ is present in the Au(I)−thiolate precursor solution and nanoparticle analysis.

A plausible fragmentation mechanism (Scheme 1) is an intermolecular rearrangement of the staples on the $Au_{25}(SCH_2CH_2Ph)_{18}$ nanocluster to form the Au_4X_4 moiety before it fragments from the nanocluster. The $Au_{21}X_{14}$ product ion can undergo a further intramolecular rearrangement to eliminate another Au_4X_4 moiety to form $Au_{17}X_{10}$ species. The Au_4X_4 is not observed di-

$$[Au_{25}SR_{18}]^{-/+} \rightarrow [Au_{21}X_{14}]^{-/+} + [Au_4X_4]^0 \rightarrow [Au_{17}X_{10}]^{-/+} + [Au_4X_4]^0 \rightarrow Au_{13}\ core\ fragments$$

$$[Au_{25}SR_{18}]^- \rightarrow [Au_{25-x}(SR)_{18-(x+1)}]^0 + [Au_x(SR)_{x+1}]^-$$

Scheme 1. Plausible fragmentation mechanism deduced from the mass spectra. The most intense peaks can be written as the basic types, $Au_{21}X_{14}$, $Au_{17}X_{10}$, $Au_x(SR)_{x+1}$, where X represents either SCH_2CH_2Ph or S.

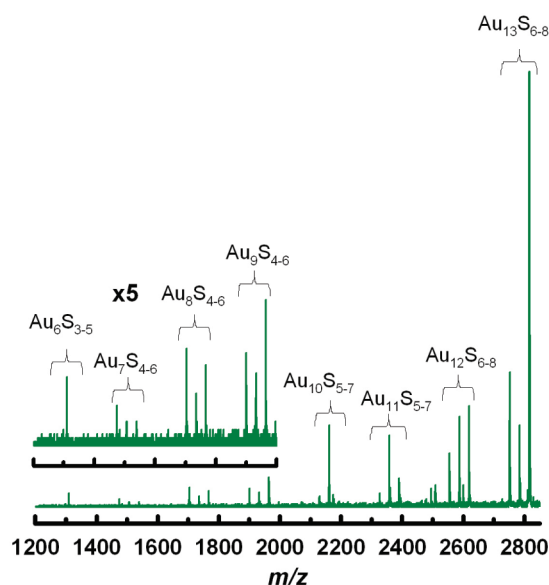**Figure 5.** The negative MS/MS spectrum of $Au_{25}(SCH_2CH_2Ph)_{18}$ corresponding to the Au_{13} core. The spectrum shows small groups associated with negatively charged ions of the form $Au_lS_m^-$. For example, the three peaks associated with the label $Au_{13}S_{6-8}$, are $Au_{13}S_8^-$, $Au_{13}S_7^-$, and $Au_{13}S_6^-$.

rectly in the MS here as it is a neutral fragment but was observed in the earlier CID study[18] due to cationization of the PEG ligand.

Stability of the Nanocluster and the Fragments: Electronic *versus* Geometric Factors. The stability of certain nanoclusters of specific charge states such as $Au_{102}(SR)_{44}$ and $Au_{25}(SR)_{18}^-$ is correlated to electronic stability[60,61] according to the formula, $n_e = N_{Au} - M_{SR} + z$ where n_e is the number of free valence-conduction electrons in the nanocluster, N_{Au} is the number of gold atoms, M_{SR} is the number of ligands and z is the charge state of the nanocluster. The fragments $Au_{25-4x}X_{18-4x}^-$ and $Au_{25-x}(SR)_{18-(x+1)}$ are dictated by the electron shell closing of 8. However, the $Au_{25}(SR)_{18}$ and its fragments of the type
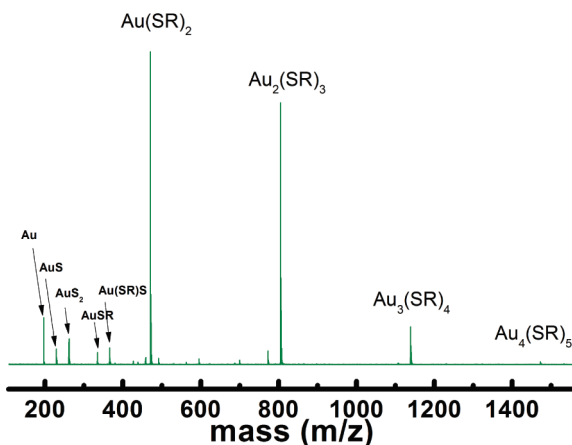

Figure 6. Low mass region of the negative IM-MS/MS spectrum of $Au_{25}(SCH_2CH_2Ph)_{18}^-$ showing the $Au(SR)_2^-$, $Au_2(SR)_3^-$, $Au_3(SR)_4^-$ and $Au_4(SR)_5^-$ species that correspond to the formation of the neutral species $Au_{24}(SR)_{16}$, $Au_{23}(SR)_{15}$, $Au_{22}(SR)_{14}$, and $Au_{21}(SR)_{13}$, respectively.

$Au_{25-4x}X_{18-4x}^+$ have an electron count of 6. Moreover, many of the products from the IM-MS/MS analysis show an electron count of $n = 8$ and 6 in negative and positive mode, respectively. Table 1 summarizes some of the main products with their corresponding electron count, and Figure 4 shows the electron count of the fragments in the MS/MS spectra. The observation of both 8 and 6 electron counts for the parent ion and fragments of the $Au_{25}(SR)_{18}$ nanocluster shows the limited nature of the electronic stability model.

Fragmentation of the Au_{13} Core. Figure 1 shows that below band 8 there is a vertical band, labeled c, which represents the fragmentation of the Au_{13} core. The product ions are not well resolved by the ion mobility separation because the loss of the Au and S atoms does not change the cross section of the nanocluster substantially. These peaks are still identifiable by their m/z and isotope patterns. Ion intensity is weak in this region and Figure 5 shows a MS/MS optimized to maximize the products of this 1200−2850 m/z region. Figure 5 shows the MS/MS mainly contains a series of ions of the form $Au_lS_n^-$ reminiscent of the pattern observed in FAB[17] that falls between the $Au_{13}S_8^-$ ion at 2816 m/z and $Au_6S_3^-$ at 1278 m/z. The ions $Au_{10}(SR)_3S_4^-$ and $Au_{11}(SR)S_6^-$ are also observed at 2509 m/z and 2496 m/z, respectively.

$Au_xL_{x+1}^-$ and Corresponding $Au_{25-x}(SR)_{18-(x+1)}$ Fragments. Figure 1 shows a series of strong peaks associated with small anionic fragments, designated d, below 1200 m/z. A close-up of the 150−1250 m/z low mass region of the negative IM-MS/MS is shown in Figure 6 and displays the species $Au(SR)_2^-$, $Au_2(SR)_3^-$, $Au_3(SR)_4^-$, and $Au_4(SR)_5^-$ in decreasing order of signal intensity, where the $Au_2(SR)_3^-$ species represents the negatively charged "staple".[62] The large neutral fragments that correspond to these are $Au_{24}(SR)_{16}$, $Au_{23}(SR)_{15}$, $Au_{22}(SR)_{14}$, and $Au_{21}(SR)_{13}$, respectively. These large fragments are neutral species and do not appear in the mass spectrum. However, $[Na_3Au_{24}(SR)_{16}]^{3+}$ was observed in Murray's[18] CID MS/MS study of $Na_xAu_{25}(SCH_2CH_2Ph)_{18-y}(S(C_2H_4O)_5CH_3)_y$. Table 1 summarizes these products with their corresponding neutral fragments. Small Au(I) thiolate species have been investigated both experimentally[63−75] and theoretically.[53] The smaller fragments observed in this study of $Au(SR)_2^-$, $Au_2(SR)_3^-$, $Au_3(SR)_4^-$, and $Au_4(SR)_5^-$ decrease in intensity as the size increases. It is likely that a cyclic, neutral Au_4L_4 fragment is more stable compared to both $Au_3(SR)_4^-$ and $Au_4(SR)_5^-$ because of the lower energetics that favor Au_4L_4 ring formation. These $Au_xL_{x+1}^-$ type fragments are not observed in the positive mode.

CID Fragmentation of $Au_{25}(SCH_2CH_2Ph)_{18}^-$ at Different Collision Energies. To demonstrate the effect of collision energy (CE) on the fragmentation of $Au_{25}(SCH_2CH_2Ph)_{18}^-$, Figure 7 shows the negative MS/MS spectra at various trap CE. As the collisional energy (CE) is increased, first the "staples" are fragmented and then the Au_{13} core. At 50
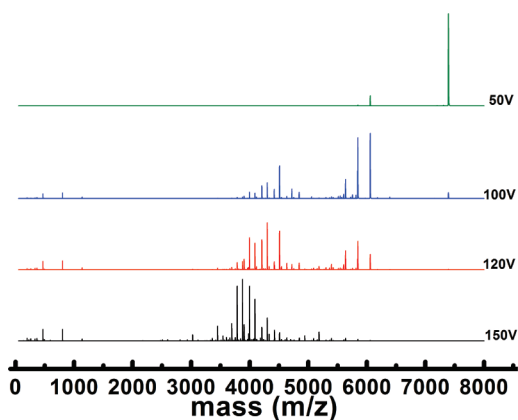
Figure 7. MS/MS of Au$_{25}$(SCH$_2$CH$_2$Ph)$_{18}$$^-$ at the different collision energies as shown in the figure. Note that these are MS/MS experiments and are not extracted from IM-MS spectra.

V, the parent ion is the predominant species with very little fragmentation. At 100 V, the parent ion is diminished substantially while the Au$_{21}$X$_{14}$$^-$ set of peaks dominate. At 120 V, the parent ion is fragmented, and there is a predominance of the Au$_{17}$X$_{10}$$^-$ type species. At 150 V CE, the fragmentation reaches the core. It is interesting to note that the core fragments do not display electron shell closing. Grönbeck, *et al.* compared the Au–Au cohesion *versus* the Au–S bond strength in the case of cyclic thiolates and concluded that the former is weaker than the latter.[53] In Figure 7, between the CE's of 120 and 150 V, the majority of the staples are stripped, and the fragmentation reaches the core. This provides a case test for comparing the Au–Au cohesion and Au–S bond strength in Au$_{25}$. At the outset, the Au–Au cohesion does appear to be stronger compared to the Au–S bond strength because the Au$_{13}$ core fragmentation appears after the Au$_{17}$X$_{10}$$^-$ type species. However, the majority of the Au–S protecting layer probably has to be removed first before the Au–Au core becomes exposed and fragmentation can occur.

CONCLUSIONS

IM-MS/MS of the Au$_{25}$(SCH$_2$CH$_2$Ph)$_{18}$ nanocluster has been obtained for the first time. The results are consistent with Au$_{25}$(SCH$_2$CH$_2$Ph)$_{18}$$^-$ existing as one structural isomer—the Au$_{13}$ core with six −SR−Au−SR−Au−SR− staples—as shown by the XRD study. The IM-MS/MS driftscope plot shows the dominant loss of one and two Au$_4$L$_4$ units with and without other additional -SCH$_2$CH$_2$Ph ligands or −CH$_2$CH$_2$Ph ligand fragments. Furthermore, the IM-MS/MS reveals the formation of a series of eight bands that are related to the fragmentation of the outer protecting "staples" shell. Each of the consecutive eight bands contains an increasing variety of Au$_l$S$_m$R$_n$$^-$ product ions due to the incremental fragmentation of the outer protective layer of Au$_{21}$X$_{14}$$^-$. The mobility of species in each individual band shows the lower mass species exhibit greater collision cross sections, due to Au and S atoms being replaced by −CH$_2$CH$_2$Ph groups. The ion mobility separation facilitates in the identification of the Au$_l$S$_m$R$_n$$^-$ products contained in the bands. Below the bands, in the region 1200 to 2800 m/z, product ions relating to the fragmentation of the Au$_{13}$ core can be observed. In the low mass 50 to 1200 m/z region, fragment ions such as Au(SR)$_2$$^-$, Au$_2(SR)_3$$^-$, Au$_3(SR)_4$$^-$, and Au$_4(SR)_5$$^-$ are also observed, corresponding to the large fragments Au$_{25-x}$(SR)$_{18-(x+1)}$. The study shows that most of the dominant large fragments are of the general type Au$_{21}$X$_{14}$$^{\mp}$, and Au$_{17}X_{10}$$^{\mp}$ with electron counts of 8 and 6 in negative and positive mode, respectively. This suggests that geometric factors may outweigh electronic factors in the selection of Au$_{25}$(SR)$_{18}$ structure. Future challenges include applying the IM-MS/MS technique for determining the arrangement of atoms in the other-sized nanoclusters.

METHODS

Materials. Tetraoctylammonium bromide (Acros, 98%), dichloromethane (Fisher, 99.99%), acetonitrile (Fisher, ≥99.9%), methanol (Fisher, 99.9%), sodium borohydride (Aldrich, 98.5%) were used as received. For the IM-MS analysis, toluene (Fox-Chemicals GmbH) and acetonitrile (Fisher, optima grade) were used.

Au$_{25}$(SCH$_2$CH$_2$Ph)$_{18}$ Preparation.[3] A colorless tetraoctylammonium bromide solution (1.01 g in 75 mL of CH$_2$Cl$_2$) was mixed with a yellow HAuCl$_4$ solution (0.503 g in 20 mL of distilled H$_2$O) and stirred vigorously until a complete phase transfer occurs. The colorless aqueous phase was separated and discarded. To the orange colored organic phase was added 0.53 mL of phenylethane thiol, and the mixture was stirred vigorously (∼30 min) until the solution became colorless. This solution was cooled in an ice bath, and a solution of NaBH$_4$ (0.513 g in 20 mL of ice cold H$_2$O) was added and stirred vigorously for 30 min. The reaction mixture was washed with an equal volume of water three times, and the solvents were removed by rotary evaporation. The oily black mixture was washed with methanol three times to remove excess thiol. The resulting black solid was coated as a thin film on a round-bottom flask during rotary evaporation.

Au$_{25}$(SCH$_2$CH$_2$Ph)$_{18}$ was obtained by multiple CH$_3$CN (∼30 mL) extractions and washed with CH$_3$OH to remove excess tetraoctylammonium bromide.

ESI-IM-MS/MS Analyses. Dry 2−5 mg samples of Au$_{25}$(SCH$_2$CH$_2$Ph)$_{18}$ were dissolved in 2−4 mL of toluene before adding 1−4 mL of acetonitrile. The sample was directly infused into the ESI source of a Synapt HDMS (Waters UK Ltd., Manchester, UK) using a flow rate of 10−40 μL/min. The hybrid instrument has a quadrupole−ion mobility−orthogonal time-of-flight configuration.[43] The ion mobility is part of the interaction region that comprises three traveling wave (T-wave) ion guides.[44] The trap T-wave functions as both a collision cell for collision-induced dissociation (CID) and as a storage cell for gating ions into the ion mobility T-wave ion guide. The IM T-wave operates by the superimposition of traveling wave voltages on a radially confining radio frequency field. In a typical experiment the traveling wave height was linearly ramped from 10 to 30 V and the wave velocity from 280 to 400 m/s for every pass along the IM T-wave ion guide. Typical pressures inside the IM cell was 0.4 mbar supplied by N$_2$ flow of 15 mL/min. The elevated pressures caused the less mobile ions to have longer drift times because

they are less effectively pushed through the IM T-wave ion guide by the traveling waves. The transfer T-wave was operated with a constant 140 m/s wave velocity and 10 V wave height to maintain the ion mobility separation from the IM T-wave cell. Both trap and the transfer ion guides were operated at pressures between $2.0-3.0 \times 10^{-2}$ mbar supplied by a 3.0–3.5 mL/min Argon flow. A range of instrument parameters were assessed for their effect on the IM-MS/MS of $Au_{25}(SCH_2CH_2Ph)_{18}$. Typical conditions in the source region were 3–4 kV capillary voltage, 80 V sampling cone, 6.0 V extraction cone, and a desolvation gas flow of 0–100 mL/min N_2. The source and desolvation temperatures were set at 100 and 210 °C, respectively. The acceleration voltages applied to the first lens in the trap and transfer ion guides control both the efficiency of transmitting ions through the instrument and the collision energy (CE) for CID experiments. Applying 20 and 18 V to the trap and transfer cells, respectively, maximized the sensitivity of the instrument and induced only negligible fragmentation of $Au_{25}(SCH_2CH_2Ph)_{18}^-$. For CID experiments, efficient fragmentation of $Au_{25}(SCH_2CH_2Ph)_{18}^-$ was achieved by increasing the voltage applied to either the trap or transfer cell. Using only the trap cell, however, for CID ensures that all product ions are separated by the IM cell. For a typical CID IM-MS, the parent ion $Au_{25}(SCH_2CH_2Ph)_{18}^-$ was accelerated by 100–200 V lab kinetic energy into the trap T-wave cell. IM-MS/MS were recorded both by resolving the $Au_{25}(SCH_2CH_2Ph)_{18}^-$ parent ion with the quadrupole or with no prior separation (Supporting Information). For CID MS/MS, 50–150 V CE was applied to the trap cell. Generally, CID with IM-MS/MS needed higher CE than CID using MS/MS alone to observe the same extent of product ion formation from the dissociation of $Au_{25}(SCH_2CH_2Ph)_{18}^-$. Low-energy collisions between the product ions and the buffer gas in the ion mobility cell may help to remove excess energy from the ions and reduce secondary fragmentation. Source fragmentation of $Au_{25}(SCH_2CH_2Ph)_{18}$ could be induced by applying 150–200 V to the sampling cone and 8.0–10.0 V to the extraction cone. The distribution of product ions formed by source or trap dissociation were similar in nature. For the MS/MS analysis of the CE dependence of product ions the transfer CE was held constant at 18 V and the trap CE was increased. Isotopic mass is used instead of the average mass throughout this work. For example, the isotopic and average mass of $Au_{25}(SCH_2CH_2Ph)_{18}$ are 7391 and 7394 Da, respectively.

Supporting Information Available: Expanded mass spectra, fragment peak assignments, and instrument layout included. This material is available free of charge *via* the Internet at http://pubs.acs.org.

REFERENCES AND NOTES

1. Whetten, R. L.; Khoury, J. T.; Alvarez, M. M.; Murthy, S.; Vezmar, I.; Wang, Z. L.; Stephens, P. W.; Cleveland, C. L.; Luedtke, W. D.; Landman, U. Nanocrystal Gold Molecules. *Adv. Mater.* **1996**, *8*, 428–433.
2. Murray, R. W. Nanoelectrochemistry: Metal Nanoparticles, Nanoelectrodes, and Nanopores. *Chem. Rev.* **2008**, *108*, 2688–2720.
3. Heaven, M. W.; Dass, A.; White, P. S.; Holt, K. M.; Murray, R. W. Crystal Structure of the Gold Nanoparticle $[N(C_8H_{17})_4][Au_{25}(SCH_2CH_2Ph)_{18}]$. *J. Am. Chem. Soc.* **2008**, *130*, 3754–3755.
4. Shichibu, Y.; Negishi, Y.; Tsunoyama, H.; Kanehara, M.; Teranishi, T.; Tsukuda, T. Extremely High Stability of Glutathionate-Protected Au_{25} Clusters against Core Etching. *Small* **2007**, *3*, 835–839.
5. Zhu, M.; Aikens, C. M.; Hollander, F. J.; Schatz, G. C.; Jin, R. Correlating the Crystal Structure of a Thiol-Protected Au_{25} Cluster and Optical Properties. *J. Am. Chem. Soc.* **2008**, *130*, 5883–5885.
6. Zhu, M. Z.; Aikens, C. M.; Hendrich, M. P.; Gupta, R.; Qian, H. F.; Schatz, G. C.; Jin, R. C. Reversible Switching of Magnetism in Thiolate-Protected Au_{25} Superatoms. *J. Am. Chem. Soc.* **2009**, *131*, 2490–2492.
7. Jiang, D.-e.; Whetten, R. L. Magnetic Doping of a Thiolated-Gold Superatom: First-Principles Density Functional Theory Calculations. *Phys. Rev. B* **2009**, *80*, 115402.
8. Si, S.; Gautier, C.; Boudon, J.; Taras, R.; Gladiali, S.; Bürgi, T. Ligand Exchange on Au_{25} Cluster with Chiral Thiols. *J. Phys. Chem. C* **2009**, *113*, 12966–12969.
9. Sànchez-Castillo, A.; Noguez, C.; Garzòin, I. L. On the Origin of the Optical Activity Displayed by Chiral-Ligand-Protected Metallic Nanoclusters. *J. Am. Chem. Soc.* **2010**, *132*, 1504–1505.
10. Retnakumari, A.; Setua, S.; Menon, D.; Ravindran, P.; Muhammed, H.; Pradeep, T.; Nair, S.; Koyakutty, M. Molecular-Receptor-Specific, Nontoxic, Near-Infrared-Emitting Au Cluster-Protein Nanoconjugates for Targeted Cancer Imaging. *Nanotechnology* **2010**, *21*, 055103.
11. Zhu, Y.; Qian, H.; Drake, B. A.; Jin, R. Atomically Precise $Au_{25}(SR)_{18}$ Nanoparticles as Catalysts for the Selective Hydrogenation of α,β-Unsaturated Ketones and Aldehydes. *Angew. Chem., Int. Ed.* **2010**, *49*, 1295–8.
12. Liu, Y.; Tsunoyama, H.; Akita, T.; Tsukuda, T. Efficient and Selective Epoxidation of Styrene with TBHP Catalyzed by Au_{25} Clusters on Hydroxyapatite. *Chem. Commun.* **2010**, *46*, 550–552.
13. Negishi, Y.; Nobusada, K.; Tsukuda, T. Glutathione-Protected Gold Clusters Revisited: Bridging the Gap between Gold(I)-Thiolate Complexes and Thiolate-Protected Gold Nanocrystals. *J. Am. Chem. Soc.* **2005**, *127*, 5261–5270.
14. Tracy, J. B.; Kalyuzhny, G.; Crowe, M. C.; Balasubramanian, R.; Choi, J. P.; Murray, R. W. Poly(ethylene glycol) Ligands for High-Resolution Nanoparticle Mass Spectrometry. *J. Am. Chem. Soc.* **2007**, *129*, 6706–6707.
15. Tracy, J. B.; Crowe, M. C.; Parker, J. F.; Hampe, O.; Fields-Zinna, C. A.; Dass, A.; Murray, R. W. Electrospray Ionization Mass Spectrometry of Uniform and Mixed Monolayer Nanoparticles: $Au_{25}[S(CH_2)_2Ph]_{18}$ and $Au_{25}[S(CH_2)_2Ph]_{18-x}(SR)_x$. *J. Am. Chem. Soc.* **2007**, *129*, 16209–16215.
16. Dass, A.; Stevenson, A.; Dubay, G. R.; Tracy, J. B.; Murray, R. W. Nanoparticle MALDI-TOF Mass Spectrometry without Fragmentation: $Au_{25}(SCH_2CH_2Ph)_{18}$ and Mixed Monolayer $Au_{25}(SCH_2CH_2Ph)_{18-x}(L)_x$. *J. Am. Chem. Soc.* **2008**, *130*, 5940–5946.
17. Dass, A.; Dubay, G. R.; Fields-Zinna, C. A.; Murray, R. W. FAB Mass Spectrometry of $Au_{25}(SR)_{18}$ Nanoparticles. *Anal. Chem.* **2008**, *80*, 6845–6849.
18. Fields-Zinna, C. A.; Sampson, J. S.; Crowe, M. C.; Tracy, J. B.; Parker, J. F.; deNey, A. M.; Muddiman, D. C.; Murray, R. W. Tandem Mass Spectrometry of Thiolate-Protected Au Nanoparticles $Na_xAu_{25}(SC_2H_4Ph)_{18-y}(S(C_2H_4O)_5CH_3)_y$. *J. Am. Chem. Soc.* **2009**, *131*, 13844–13851.
19. Harkness, K. M.; Cliffel, D. E.; McLean, J. A. Characterization of Thiolate-Protected Gold Nanoparticles by Mass Spectrometry. *Analyst* **2010**, *135*, 868–874.
20. Chaki, N. K.; Negishi, Y.; Tsunoyama, H.; Shichibu, Y.; Tsukuda, T. Ubiquitous 8 and 29 kDa Gold: Alkanethiolate Cluster Compounds: Mass-Spectrometric Determination of Molecular Formulas and Structural Implications. *J. Am. Chem. Soc.* **2008**, *130*, 8608–8610.
21. Qian, H.; Jin, R. Controlling Nanoparticles with Atomic Precision: The Case of $Au_{144}(SCH_2CH_2Ph)_{60}$. *Nano Lett.* **2009**, *9*, 4083–4087.
22. Fields-Zinna, C. A.; Sardar, R.; Beasley, C. A.; Murray, R. W. Electrospray Ionization Mass Spectrometry of Intrinsically Cationized Nanoparticles, $[Au_{144/146}(SC_{11}H_{22}N(CH_2CH_3)_3{}^+)_x(S(CH_2)_5CH_3)_y]^{x+}$. *J. Am. Chem. Soc.* **2009**, *131*, 16266–16271.
23. Jadzinsky, P. D.; Calero, G.; Ackerson, C. J.; Bushnell, D. A.; Kornberg, R. D. Structure of a Thiol Monolayer-Protected Gold Nanoparticle at 1.1 Angstrom Resolution. *Science* **2007**, *318*, 430–433.

24. Qian, H.; Eckenhoff, W. T.; Zhu, Y.; Pintauer, T.; Jin, R. Total Structure Determination of Thiolate-Protected Au_{38} Nanoparticles. *J. Am. Chem. Soc.* **2010**, *132*, 8280–8281.

25. Akola, J.; Walter, M.; Whetten, R. L.; Hakkinen, H.; Gronbeck, H. On the Structure of Thiolate-Protected Au_{25}. *J. Am. Chem. Soc.* **2008**, *130*, 3756–3757.

26. Iwasa, T.; Nobusada, K. Theoretical Investigation of Optimized Structures of Thiolated Gold Cluster $[Au_{25}(SCH_3)_{18}]^+$. *J. Phys. Chem. C* **2007**, *111*, 45–49.

27. Wu, Z.; Gayathri, C.; Gil, R. R.; Jin, R. Probing the Structure and Charge State of Glutathione-Capped $Au_{25}(SG)_{18}$ Clusters by NMR and Mass Spectrometry. *J. Am. Chem. Soc.* **2009**, *131*, 6535–6542.

28. Pringle, S. D.; Giles, K.; Wildgoose, J. L.; Williams, J. P.; Slade, S. E.; Thalassinos, K.; Bateman, R. H.; Bowers, M. T.; Scrivens, J. H. An Investigation of the Mobility Separation of Some Peptide and Protein Ions using a New Hybrid Quadrupole/ Travelling Wave IMS/oa-TOF Instrument. *Int. J. Mass Spectrom.* **2007**, *261*, 1–12.

29. Gies, A. P.; Kliman, M.; McLean, J. A.; Hercules, D. M. Characterization of Branching in Aramid Polymers Studied by MALDI-Ion Mobility/Mass Spectrometry. *Macromolecules* **2008**, *41*, 8299–8301.

30. Trimpin, S.; Plasencia, M.; Isailovic, D.; Clemmer, D. E. Resolving Oligomers from Fully Grown Polymers with IMS-MS. *Anal. Chem.* **2007**, *79*, 7965–7974.

31. Trimpin, S.; Clemmer, D. E. Ion Mobility Spectrometry/Mass Spectrometry Snapshots for Assessing the Molecular Compositions of Complex Polymeric Systems. *Anal. Chem.* **2008**, *80*, 9073–9083.

32. Hilton, G. R.; Jackson, A. T.; Thalassinos, K.; Scrivens, J. H. Structural Analysis of Synthetic Polymer Mixtures Using Ion Mobility and Tandem Mass Spectrometry. *Anal. Chem.* **2008**, *80*, 9720–9725.

33. Chan, Y.-T.; Li, X.; Soler, M.; Wang, J.-L.; Wesdemiotis, C.; Newkome, G. R. Self-Assembly and Traveling Wave Ion Mobility Mass Spectrometry Analysis of Hexacadmium Macrocycles. *J. Am. Chem. Soc.* **2009**, *131*, 16395–16397.

34. Anderson, S. E.; Bodzin, D. J.; Haddad, T. S.; Boatz, J. A.; Mabry, J. M.; Mitchell, C.; Bowers, M. T. Structural Investigation of Encapsulated Fluoride in Polyhedral Oligomeric Silsesquioxane Cages Using Ion Mobility Mass Spectrometry and Molecular Mechanics. *Chem. Mater.* **2008**, *20*, 4299–4309.

35. Williams, J. P.; Grabenauer, M.; Holland, R. J.; Carpenter, C. J.; Wormald, M. R.; Giles, K.; Harvey, D. J.; Bateman, R. H.; Scrivens, J. H.; Bowers, M. T. Characterization of Simple Isomeric Oligosaccharides and the Rapid Separation of Glycan Mixtures by Ion Mobility Mass Spectrometry. *Int. J. Mass Spectrom.*, published online August 28, 2009, http://dx.doi.org/10.1016/j.ijms. 2009.08.006.

36. Smith, D. P.; Giles, K.; Bateman, R. H.; Radford, S. E.; Ashcroft, A. E. Monitoring Copopulated Conformational States During Protein Folding Events Using Electrospray Ionization-Ion Mobility Spectrometry-Mass Spectrometry. *J. Am. Soc. Mass. Spectrom.* **2007**, *18*, 2180–2190.

37. Hopper, J. T. S.; Oldham, N. J. Collision Induced Unfolding of Protein Ions in the Gas Phase Studied by Ion Mobility-Mass Spectrometry: The Effect of Ligand Binding on Conformational Stability. *J. Am. Soc. Mass. Spectrom.* **2009**, *20*, 1851–1858.

38. Murray, M. M.; Bernstein, S. L.; Nyugen, V.; Condron, M. M.; Teplow, D. B.; Bowers, M. T. Amyloid β Protein: Aβ40 Inhibits Aβ42 Oligomerization. *J. Am. Chem. Soc.* **2009**, *131*, 6316–6317.

39. Zilch, L. W.; Kaleta, D. T.; Kohtani, M.; Krishnan, R.; Jarrold, M. F. Folding and Unfolding of Helix-Turn-Helix Motifs in the Gas Phase. *J. Am. Soc. Mass. Spectrom.* **2007**, *18*, 1239–1248.

40. Benesch, J. L. P. Collisional Activation of Protein Complexes: Picking Up the Pieces. *J. Am. Soc. Mass. Spectrom.* **2009**, *20*, 341–348.

41. Jackson, S. N.; Ugarov, M.; Post, J. D.; Egan, T.; Langlais, D.; Schultz, J. A.; Woods, A. S. A Study of Phospholipids by Ion Mobility TOFMS. *J. Am. Soc. Mass. Spectrom* **2008**, *19*, 1655–1662.

42. Ruotolo, B. T.; Benesch, J. L. P.; Sandercock, A. M.; Hyung, S.-J.; Robinson, C. V. Ion Mobility-Mass Spectrometry Analysis of Large Protein Complexes. *Nat. Protocols* **2008**, *3*, 1139–1152.

43. Ridenour, W. B.; Kliman, M.; McLean, J. A.; Caprioli, R. M. Structural Characterization of Phospholipids and Peptides Directly from Tissue Sections by MALDI Traveling-Wave Ion Mobility-Mass Spectrometry. *Anal. Chem.* **2010**, *82*, 1881–1889.

44. Ruotolo, Brandon, T.; Hyung, S.-J.; Robinson, Paula, M.; Giles, K.; Bateman, Robert, H.; Robinson, Carol, V. Ion Mobility-Mass Spectrometry Reveals Long-Lived, Unfolded Intermediates in the Dissociation of Protein Complexes. *Angew. Chem., Int. Ed.* **2007**, *46*, 8001–8004.

45. Valentine, S. J.; Plasencia, M. D.; Liu, X.; Krishnan, M.; Naylor, S.; Udseth, H. R.; Smith, R. D.; Clemmer, D. E. Toward Plasma Proteome Profiling with Ion Mobility-Mass Spectrometry. *J. Proteome Res.* **2006**, *5*, 2977–2984.

46. Giles, K.; Pringle, S. D.; Worthington, K. R.; Little, D.; Wildgoose, J. L.; Bateman, R. H. Applications of a Travelling Wave-Based Radio-Frequency-Only Stacked Ring Ion Guide. *Rapid Commun. Mass Spectrom.* **2004**, *18*, 2401–2414.

47. Harkness, K. M.; Fenn, L. S.; Cliffel, D. E.; McLean, J. A. Surface Fragmentation of Complexes from Thiolate Protected Gold Nanoparticles by Ion Mobility-Mass Spectrometry. *Anal. Chem.* **2010**, *82*, 3061–3066.

48. Negishi, Y.; Chaki, N. K.; Shichibu, Y.; Whetten, R. L.; Tsukuda, T. Origin of Magic Stability of Thiolated Gold Clusters: A Case Study on $Au_{25}(SC_6H_{13})_{18}$. *J. Am. Chem. Soc.* **2007**, *129*, 11322–11323.

49. Shvartsburg, A. A.; Smith, R. D. Fundamentals of Traveling Wave Ion Mobility Spectrometry. *Anal. Chem.* **2008**, *80*, 9689–9699.

50. Dass, A. Mass Spectrometric Identification of $Au_{68}(SR)_{34}$ Molecular Gold Nanoclusters with 34-Electron Shell Closing. *J. Am. Chem. Soc.* **2009**, *131*, 11666–11667.

51. Dharmaratne, A. C.; Krick, T.; Dass, A. Nanocluster Size Evolution Studied by Mass Spectrometry in Room Temperature $Au_{25}(SR)_{18}$ Synthesis. *J. Am. Chem. Soc.* **2009**, *131*, 13604–13605.

52. Rinehart, K. L. J. Fast Atom Bombardemnt Mass Spectrometry. *Science* **1982**, 218.

53. Gronbeck, H.; Walter, M.; Hakkinen, H. Theoretical Characterization of Cyclic Thiolated Gold Clusters. *J. Am. Chem. Soc.* **2006**, *128*, 10268–10275.

54. Hakkinen, H.; Walter, M.; Gronbeck, H. Divide and Protect: Capping Gold Nanoclusters with Molecular Gold-Thiolate Rings. *J. Phys. Chem. B* **2006**, *110*, 9927–9931.

55. Gies, A. P.; Hercules, D. M.; Gerdon, A. E.; Cliffel, D. E. Electrospray Mass Spectrometry Study of Tiopronin Monolayer-Protected Gold Nanoclusters. *J. Am. Chem. Soc.* **2007**, *129*, 1095–1104.

56. Zhang, Y.; Shuang, S.; Dong, C.; Lo, C. K.; Paau, M. C.; Choi, M. M. F. Application of HPLC and MALDI-TOF MS for Studying As-Synthesized Ligand-Protected Gold Nanoclusters Products. *Anal. Chem.* **2009**, *81*, 1676–1685.

57. Negishi, Y.; Tsukuda, T. One-Pot Preparation of Subnanometer-Sized Gold Clusters *via* Reduction and Stabilization by *meso*-2,3-Dimercaptosuccinic Acid. *J. Am. Chem. Soc.* **2003**, *125*, 4046–4047.

58. Tang, Z.; Xu, B.; Wu, B.; Germann, M. W.; Wang, G. Synthesis and Structural Determination of Multidentate 2,3-Dithiol-Stabilized Au Clusters. *J. Am. Chem. Soc.* **2010**, *132*, 3367–3374.

59. Qian, H.; Zhu, Y.; Jin, R. Isolation of Ubiquitous $Au_{40}(SR)_{24}$ Clusters from the 8 kDa Gold Clusters. *J. Am. Chem. Soc.* **2010**, *132*, 4583–4585.

60. Walter, M.; Akola, J.; Lopez-Acevedo, O.; Jadzinsky, P. D.; Calero, G.; Ackerson, C. J.; Whetten, R. L.; Gronbeck, H.;

Hakkinen, H. A Unified View of Ligand-Protected Gold Clusters as Superatom Complexes. *Proc. Natl. Acad. Sci. U.S.A.* **2008**, *105*, 9157–9162.

61. Wyrwas, R. B.; Alvarez, M. M.; Khoury, J. T.; Price, R. C.; Schaaff, T. G.; Whetten, R. L. The Colours of Nanometric Gold—Optical Response Functions of Selected Gold-Cluster Thiolates. *Eur. Phys. J. D* **2007**, *43*, 91–95.

62. Schaaff, T. G. Laser Desorption and Matrix-Assisted Laser Desorption/Ionization Mass Spectrometry of 29-kDa Au: SR Cluster Compounds. *Anal. Chem.* **2004**, *76*, 6187–6196.

63. Canumalla, A. J.; Al-Zamil, N.; Phillips, M.; Isab, A. A.; Shaw Iii, C. F. Redox and Ligand Exchange Reactions of Potential Gold(I) and Gold(III)-Cyanide Metabolites under Biomimetic Conditions. *J. Inorg. Biochem.* **2001**, *85*, 67–76.

64. Corbierre, M. K.; Lennox, R. B. Preparation of Thiol-Capped Gold Nanoparticles by Chemical Reduction of Soluble Au(I)-Thiolates. *Chem. Mater.* **2005**, *17*, 5691–5696.

65. Dance, I. G. The Structural Chemistry of Metal Thiolate Complexes. *Polyhedron* **1986**, *5*, 1037–1104.

66. LeBlanc, D. J.; Smith, R. W.; Wang, Z. X.; HowardLock, H. E.; Lock, C. J. L. Thiomalate Complexes of Gold(I): Preparation, Characterization, and Crystal Structures of 1:2 Gold to Thiomalate Complexes. *J. Chem. Soc., Dalton Trans.* **1997**, 3263–3267.

67. LeBlanc, D. J.; Lock, C. J. L. Cyclo-hexakis[(2,4,6-triisopropylthio-phenolato-S:S)gold(I)] Diethyl Ether Solvate. *Acta Crystallogr. C* **1997**, *53*, 1765–1768.

68. Tong, Y. Y.; Pombeiro, A. J. L.; Hughes, D. L.; Richards, R. L. Synthesis and Properties of the Gold(I) Complexes with Bulky Thiolates [Au(SR)]$_6$ and [Au(SR)(PPh$_3$)] and the Molecular Structure of [Au(SC$_6$H$_2$PR3I-2,4,6)(PPh$_3$))]. *Transition Met. Chem.* **1995**, *20*, 372–375.

69. Bachman, R. E.; Bodolosky-Bettis, S. A.; Pyle, C. J.; Gray, M. A. Reversible Oxidative Addition and Reductive Elimination of Fluorinated Disulfides at Gold(I) Thiolate Complexes: A New Ligand Exchange Mechanism. *J. Am. Chem. Soc.* **2008**, *130*, 14303–14310.

70. Al-Sa'ady, A. K.; M, C. A.; Parish, R. V.; Sandbank, J. A. A General Synthesis for Gold(I) Complexes. *Inorg. Synth.* **1985**, *23*, 191–194.

71. Uson, R.; L, A.; Laguna, M. (Tetrahydrothiophene)gold(I) or Gold(III) Complexes. *Inorg. Synth.* **1989**, *26*, 85–91.

72. Brinas, R. P.; Hu, M.; Qian, L.; Lymar, E. S.; Hainfeld, J. F. Gold Nanoparticle Size Controlled by Polymeric Au(I) Thiolate Precursor Size. *J. Am. Chem. Soc.* **2007**, *130*, 975–982.

73. Bachman, R. E.; Bodolosky-Bettis, S. A.; Glennon, S. C.; Sirchio, S. A. Formation of a Novel Luminescent Form of Gold(I) Phenylthiolate *via* Self-Assembly and Decomposition of Isonitrilegold(I) Phenylthiolate Complexes. *J. Am. Chem. Soc.* **2000**, *122*, 7146–7147.

74. Yangyuoru, P. M.; Webb, J. W.; Shaw Iii, C. F. Glutathionato-S-Gold(III) Complexes Formed as Intermediates in the Reduction of Auricyanide by Glutathione. *J. Inorg. Biochem.* **2008**, *102*, 584–593.

75. Yan, B.; Zhu, Z.-J.; Miranda, O.; Chompoosor, A.; Rotello, V.; Vachet, R. Laser Desorption/Ionization Mass Spectrometry Analysis of Monolayer-Protected Gold Nanoparticles. *Anal. Bioanal. Chem.* **2010**, *396*, 1025–1035.